Instantaneous sea ice drift speed from TanDEM-X interferometry

Dyre Oliver Dammann[1], Leif E. B. Eriksson[1], Joshua M. Jones[2], Andrew R. Mahoney[2,3], Roland Romeiser[4], Franz J. Meyer[2], Hajo Eicken[3,5], Yasushi Fukamachi[3,6,7]

[1]Department of Space, Earth, and Environment, Chalmers University of Technology, Gothenburg, Sweden
[2]Geophysical Institute, University of Alaska Fairbanks, Fairbanks, AK, USA
[3]Global Station for Arctic Research, Hokkaido University, Sapporo, Japan
[4]Rosenstiel School of Marine and Atmospheric Science, University of Miami, Miami, FL, USA
[5]International Arctic Research Center, University of Alaska Fairbanks, Fairbanks AK, USA
[6]Arctic Research Center, Hokkaido University, Sapporo, Japan
[7]Institute of Low Temperature Science, Hokkaido University, Sapporo, Japan

Correspondence to: Dyre Oliver Dammann (dyre.dammann@chalmers.se)

Abstract. The drift of sea ice is an important geophysical process with widespread implications for the ocean energy budget, ecosystems, and marine operations. Drifting sea ice can threaten navigation routes and present a hazard for ocean vessels and maritime installations. Here, we evaluate single-pass synthetic aperture radar (SAR) interferometry (InSAR) as a tool to assess ice drift for different uses. Initial validation shows that TanDEM-X phase-derived drift speed corresponds well with drift products from a ground-based radar at Utqiaġvik, Alaska. Joint analysis of TanDEM-X and Sentinel-1 data covering the Fram Strait demonstrates that InSAR can help quantify the opening/closing rate of leads. In contrast to standard SAR-based drift algorithms deriving averaged drift velocities, single-pass InSAR enables an instantaneous assessment with advantages in the context of ice management and transportation. By evaluating sea ice drift through the Vilkitsky Strait, Russia, we identified short-lived transient convergence patterns. We conclude that InSAR enables the identification of potentially important short-lived dynamic processes otherwise difficult to observe with possible implication for engineering and sea ice modeling.

1 Introduction

Arctic sea ice is predominately in a state of drift as a result of a near continual wind and ocean drag, which leads to redistribution and deformation. Drift processes play a large part in the sea ice thickness distribution. Differential ice motion results in the opening and closing of leads and polynyas and the formation of pressure ridges, while large-scale drift patterns control sea ice loss through export from the Arctic Ocean. Sea ice drift has therefore major implications for the mass, heat, and momentum balance of the Arctic Ocean's ice cover. Over the past several decades, Arctic sea ice has declined at a rapid rate (Stroeve et al., 2012;Comiso and Hall, 2014;Meier et al., 2014) and in confined regions resulted in more dynamic ice (Spreen et al., 2011;Kwok et al., 2013) increasing strain and fracturing (Rampal et al., 2009a). Recent and predicted changes in sea ice drift (Zhang et al., 2012) are impacting marine biota (Thomas, 2017) and coastal populations (Krupnik et al., 2010). Sea ice drift is also a major concern for maritime activities (Eicken et al., 2009), and associated sea ice hazards play a prominent role in offshore resource development and associated coastal infrastructure (Eicken and Mahoney, 2015).

The wide relevance across scientific disciplines and end users has resulted in numerous approaches for measuring ice drift. GPS buoys are an important tool to determine ice drift on pan-Arctic scales (Meier and Maslanik, 2003;Zhang et al., 2003;Rampal et al., 2009b) with unmatched temporal sampling, but are often hundreds of kilometers apart and cannot provide detailed km-scale information unless specifically deployed for validation purposes. Ground-based remote sensing

5   systems on the other hand, such as X-band marine radars are capable of providing consistent m-scale resolution ice drift measurements and deformation information (Druckenmiller et al., 2009;Shirasawa et al., 2013;Jones et al., 2016;Karvonen, 2016;Oikkonen et al., 2016). The coverage of ground based systems is typically limited to coastal waters, hence satellite remote sensing is also an important tool to measure ice drift (Muckenhuber and Sandven, 2017). Here, microwave systems are superior due to the ability to provide information regardless of light or atmospheric conditions. Passive systems such as

10   the Special Sensor Microwave Imager (SSM/I) are capable of providing information on the pan-Arctic scale (Kwok et al., 1998;Spreen et al., 2011) with relevance for determining sea ice age and the Arctic mass and energy budget, but with a resolution of tens of km.

Active sensors and in particular synthetic aperture radar (SAR) are capable of providing much higher resolution ice drift products at the km-scale by deriving displacement vectors between two consecutive scenes commonly through feature

15   tracking and/or pattern matching (Berg and Eriksson, 2014;Karvonen, 2016;Muckenhuber and Sandven, 2017). These methods depend on at least two consecutive SAR scenes frequently acquired days apart, such that the often-complex drift patterns of sea ice frequently lead to underestimation of ice drift speeds by 10-20% (Haller et al., 2014), but can likely be much higher (Hutchings et al., 2011). The use of a single SAR scene for estimation of instantaneous ice drift using the Doppler centroid anomaly (DCA) was therefore proposed by Kræmer et al. (2015). This technique is capable of providing

20   one-dimensional drift products in the satellite's look direction with resolution on the km-scale. However, the technique is sensitive to biases and aliasing related to the ice surface, accuracy of the satellites orbit state vectors, antenna and incidence angle. The technique further requires incorporation and manual interpretation of land areas in each scene where biases can be corrected (Kræmer et al., 2015).

All of the techniques mentioned provide valuable ice drift assessments across different spatial and temporal scales, but do

25   not provide a consistent approach with optimal m-scale resolution beneficial to support Arctic stakeholders, such as local ice use, shipping, and resource exploration (Eicken et al., 2009;Dammann et al., 2018a). Monitoring of environmental hazards and effective emergency response in sea ice environments require high-resolution data of ice hazard distributions (e.g., multiyear ice, landfast ice breakout, and ice push events), ice movement and deformation, as well as ice characteristics and dynamics relevant to emergency response (Eicken et al., 2011).

30   In this work, we explore SAR interferometry (InSAR) as a tool to provide instantaneous m-scale resolution ice drift products. InSAR is a signal processing technique which extracts the phase difference between SAR images acquired from similar viewing geometries. This interferometric phase can either signify sea ice topography if acquisitions are separated in

space (i.e. non-zero perpendicular baseline) or motion in the look direction if separated in time (non-zero temporal lag). InSAR has mainly been used to study deformation (Li et al., 1996;Dammert et al., 1998;Morris et al., 1999;Vincent et al., 2004;Meyer et al., 2011;Berg et al., 2015;Marbouti et al., 2017;Dammann et al., 2018b;Dammann et al., 2018d;Dammann et al., In review) and topography (Dammann et al., 2017;Dierking et al., 2017) of landfast sea ice since the drifting ice

5 generally moves too much between most satellite acquisitions to retain coherence over days to weeks. However, during the pursuit operation mode of TanDEM-X in 2010 and 2015, InSAR analysis of drifting ice was possible with temporal lags on the order of seconds (Scheiber et al., 2011;Mahoney et al., 2016;Dammann et al., 2018c).

The interferometric phase is represented between -π and π. Under conditions where ice floes drift linearly at slightly different velocities without rotating, each floe will feature different homogenous phase values. However, with baselines on

10 the order of seconds, floes generally rotate or slightly deform leading to non-homogenous phase values where the phase can fall outside the [–π: π] range and will "wrap around" to the opposite side of the phase cycle causing phase ambiguities. An interferogram is a visual representation of the phase and typically consist of multiple fringes (stripes) of equal phase in case of a baseline on the order of seconds or days for drifting and landfast ice, respectively. The fringes resulting from 1-dimensional phase information can be interpreted into 2-dimensional motion using inverse modeling and provide important

15 information pertaining to internal deformation of the ice (Dammann et al., 2016), but can at the same time hide a constant phase value pertaining to the general drift speed. Here, we apply bistatic acquisitions with substantially shorter (~ 10 ms) temporal lag for the evaluation of instantaneous sea ice drift speed. This technique has been used for assessment of surface current velocity (Romeiser and Thompson, 2000;Romeiser and Runge, 2007;Romeiser et al., 2010), but to our knowledge has not been used to measure sea ice drift.

20 **2 Data and methods**

2.1 Study area and validation data

We focus validation efforts over Utqiaġvik (formerly known as Barrow), situated in the eastern Chukchi Sea near Point Barrow, Alaska (Figure 1). We chose this region because of its diverse ice dynamics, the authors' direct experience with the region over the past two decades, and the ground-based radar stationed in Utqiaġvik continuously tracking sea ice drift.

25 Prevailing winds from the northeast in combination with opposing currents and the orientation of the land results in ice drift predominantly towards the southwest, persistent patches of open water, and ridged ice (Norton and Gaylord, 2004;Jones et al., 2016).

The near-shore ice out to a range of 11 km is continuously monitored using a Furuno FAR-2127 25 kW, X-band (3 cm, 10 GHz) marine radar from an altitude of 22.5 m (Figure 1). Radar images are archived every 5 m and used for monitoring

30 landfast ice, providing information on dynamics of offshore ice (Druckenmiller et al., 2009). Due to occlusions and non-rigid body deformation, traditional feature tracking methods are not always effective in tracking sea ice from marine radar

imagery. To reduce the noise of calculated motion vectors, we apply a combination of existing and newly developed methods (Rohith et al., 2013;Jones et al., 2016), leading to filtered motion products averaged over 1.5 hours. Even so, the motion tracking algorithm only produced consistent motion vectors suitable for validation in one out of three cases (Nov 21).

To assess the ocean currents in the vicinity of our study area, we analyzed data from two moorings, M1 and M2, deployed
5   near Utqiaġvik at 71.204N, 157.680W and 71.813N, 156.675W at a water depth of 53 m and 70 m respectively (Figure 1). The moorings contained a Teledyne RDI Workhorse Sentinel acoustic Doppler current profiler (ADCP), whose data we use to evaluate surface current velocity (Mahoney et al., 2015). Velocities are derived from the Doppler shifts of return signals from particles within the water column.

In addition to Utqiaġvik, we explore the potential of InSAR-derived ice drift in the Fram and Vilkitsky Straits. Situated by
10   the east coast of Greenland, the Fram Strait is an important location due to the dynamic conditions and large fluxes of both first- and multiyear sea ice. The Vilkitsky Strait is situated by the Taymyr Peninsula and is a strategic location on the Northern Sea Route (Arctic Council, 2009).

2.2 TanDEM-X data

The twin constellation TanDEM-X has operated since 2010, with a repeat-pass cycle of 11 days featuring two X-band ($\lambda =$
15   3.1 cm) SAR sensors. We obtained single-look complex image pairs from the German Aerospace Center (DLR). Images were acquired in stripmap bistatic mode with short along-track baselines of less than 100 m. Image information for the images used in this work can be found in Table 1. We considered the entire data set acquired by TanDEM-X over Utqiaġvik and chose to focus on three consecutive acquisitions during 30 Oct. – 21 Nov, 2015. This time span was chosen based on (1) the ground-based radar being operational, (2) less than a kilometer wide landfast ice maximizing the ground-based radar
20   footprint occupied by drifting ice, and (3) dynamic ice conditions. Due to increasingly later fall freeze-up of landfast ice near Utqiaġvik (Mahoney et al., 2014), sea ice grown in-situ is likely only a few centimeters thick during Oct. – Nov., but with potential advection of thicker ice from the eastern Beaufort Sea. The scenes were processed using a standard InSAR workflow (Bamler and Hartl, 1998;Ferretti et al., 2007;Dammann et al., 2016) including interferogram formation, adaptive phase filtering (Goldstein and Werner, 1998), and geocoding using the GAMMA software (Werner et al., 2000). The ice
25   drift was derived from the interferometric phase further described in the following section. Of the three acquisitions obtained near Utqiaġvik, only the image pair from 21 Nov. was acquired when the ground-based radar was operational and could provide a coherent motion product and was thus used for validation of the derived drift.

2.3 InSAR-derived drift speed

In an interferogram, only displacement in look-direction (Δr_{LOS}) results in a phase change $\Delta \Phi_{disp}$ according to $\Delta \Phi_{disp} =$
30   $4\pi \, \Delta r_{LOS}/\lambda$. For TanDEM-X, the sensor wavelength λ is 3.1 cm, such that ice displacement has to exceed $\Delta r_{LOS} \approx 1.5 cm$ for the $\Delta \Phi_{disp}$ phase values to "wrap around". This rarely occurs with the short interferometric time lag of roughly 10 ms

used in this work. $\Delta\Phi_{disp}$ can be converted to drift speed in look direction using the speed of ambiguity, which is the motion resulting in one phase cycle. We first calculate the ground range displacement in look direction resulting in one full phase cycle (displacement of ambiguity, d), which can be expressed:

$$d = \frac{\lambda}{2\sin\theta} \qquad (1)$$

5 where θ is the incidence angle. Furthermore, the speed of ambiguity can be expressed as $v_a = d/B_t$, where the temporal baseline $B_t = B_\parallel/v_s$, v_s is the orbit speed of the satellite (7.6 km s^{-1}), and $B_\parallel$ is the along-track baseline. The phase-derived speed in look direction is calculated as:

$$v_\phi = \frac{\Delta\Phi_{disp}}{2\pi} v_a \qquad (2)$$

The absolute phase and motion values are initially unknown; thus, we calibrate v_ϕ by subtracting the derived speed of

10 landfast ice so it is ensured to be zero. Although the direction of motion cannot be determined using the phase information alone, it is possible to determine the binary direction (i.e. whether scatterers increase or decrease their distance to the satellite) by evaluating spatially continuous phase gradients. Here, an increasing phase is indicative of increased motion towards the satellite (if the image acquired by the leading satellite is used as a master image). We further define the positive direction such that a positive v_ϕ is indicative of speed towards the satellite.

15 ## 2.4 Drift speed ambiguities

It is necessary to evaluate topography as a potential contributor to phase change. The height of ambiguity, h_a, (i.e. the elevation that would result in one phase cycle) can be expressed:

$$h_a = \frac{\lambda R \sin\theta}{m B_\perp} \qquad (3)$$

where $B_\perp$ is the perpendicular baseline, R is the slant range, and m = 1 or 2 for monostatic and bistatic acquisitions,

20 respectively. The potential resulting speed error, v_e, caused by assuming the entire phase response to be motion driven, when in reality topographic features of height h_0 are present, can be determined:

$$v_e = h_o \frac{v_a}{h_a} \qquad (4)$$

For the scenes considered here, h_a-values are roughly 40 meters hence cm-scale height offsets will result in v_e on the order of mm s^{-1}. Therefore, the height offset between floes would have to approach one meter to make a significant contribution.

25 This height offset would have to be prominent across an entire floe, which would reflect a difference in ice thickness and hence would mostly be relevant for ice bergs or thick multiyear ice. Ice ridges can often feature offsets larger than a meter,

but can easily be identified as a topographic response since they would otherwise indicate a non-homogenous motion across a floe, which is implausible at the timescales considered here.

In addition to topography, it is necessary to consider phase contributions from ocean waves in areas of young ice. The phase
5 values of rigid ice floes will not be significantly impacted by waves, but fragmented ice is capable of following the vertical motion of dm-scale wind-driven waves. The backscatter contribution from waves will often be dominated by the motion of the wave surface facing the radar. Hence, waves propagating toward the radar will result in a positive contribution to the interferometric phase due to the upward motion of the wave face seen by the radar. Conversely, waves travelling away from the radar will result in a negative phase contribution (Thompson and Jensen, 1993;Romeiser and Thompson, 2000). The
10 speed contribution from dm-scale waves is inversely proportional to the sine of the incidence angle. Hence the contribution from waves can be substantial in cases of small incidence angles and can be larger than any physical motion of the wave itself. Smaller cm-scale capillary waves can also result in a contribution to the derived speed (Valenzuela, 1978;Thompson and Jensen, 1993;Romeiser and Thompson, 2000).

3 Results

15 **3.1 Drift speed validation near Utqiaġvik, Alaska**

Three images acquired near Utqiaġvik were processed for interferometric phase and speed in look direction and displayed in Figure 2. During the time spanned by the three acquisitions, the wind direction ranged between NNE and E predominately resulting in SW ice drift along the coast. Note that we use standard atmospheric convention for winds (by referring to the direction from which the wind is coming) and the oceanographic convention for surface currents and ice drift (by referring to
20 the direction in which the ice or current is moving).

The image acquired on Oct. 30 features dispersed floes and open water and is displayed in Figure 2a. Areas of open water appear dark in the backscatter image due to low wind speed (~4 m s^{-1}) and hence low surface roughness in the form of capillary waves (see circled area in Figure 2a). The look-directional speed based on the interferometric phase is displayed in Figure 2b. Here, the exact speed has been calibrated to the known stationary ice on Elson Lagoon. Positive speed is defined
25 as the direction opposite to look-direction (roughly towards WSW). The velocity field exhibits negative (ENE) surface velocity near the coast (see "A" in Figure 2b). This can be explained by the relatively low NNE wind speed and hence the opposing Alaska Coastal Current (Ahlnäs and Garrison, 1984;Winsor and Chapman, 2004;Jones et al., 2016) becomes the dominant force of ice drift, which at the time of the acquisition was NE at 0.4 m s^{-1} as observed with mooring M1. Further off shore the speed changes orientation towards WSW, likely due to wind becoming the dominant forcing resulting in
30 convergence around the dashed line (zero velocity) at the time of the acquisition (Figure 2b). Where positive velocity, areas

of open water appears to be moving faster toward the WSW (positive direction) than the surrounding ice (top circle in Figure 2b) likely due to a wind-induced wave contribution to the phase. Here, the speed of the waves will be added to the effect of the currents resulting in apparent higher speed. Further off shore (see "B" in Figure 2b), the negative drift speed is likely due to reduced wind speed or altered wind direction since the current slowed down significantly further off shore as measured by

5   M2 (not shown).

On Nov. 10, the wind was stronger than during the other acquisitions (10 m s⁻¹) and areas of open water exhibit higher backscatter than the ice floes that were present due to wind-roughening of the surface (see circled area in in Figure 2c). The strong wind results in a consistently positive drift speed in look direction, which decreases with distance to shore (Figure 2d). This gradient was likely due to variable wind and ice forcing as the current velocity was comparable between M1 and

10   M2. In between floes, the ocean surface exhibits velocities roughly 1 m s⁻¹ larger than that of the adjacent ice. This difference in speed can be explained by wind-driven waves, which are attenuated beneath the larger floes, but will have an impact over open water and looser fragmented ice. The apparent speed increase with distance from shore within the bottom circled area in Figure 2d is consistent with dm-scale wind-driven waves in which amplitudes increase with fetch.

At the time of acquisition on Nov. 21, the sea ice in the radar footprint consisted of a mix of large floes surrounded by young

15   ice and open water (see circled areas in Figure 2e). It is apparent that the floes are largely drifting with homogenous speed in the southwest direction (positive speed defined as the direct opposite of look direction) (Figure 2f). The derived speed also exhibits a higher surface velocity in the areas of open water and thin ice between the floes (~1 m s⁻¹ vs. ~0.6 m s⁻¹) (circled area in Figure 2f), but less pronounced than on Nov. 10. This is likely due to reduced wind speed (7 m s⁻¹) and the presence of young ice in between floes (circled area in Figure 2e) damping the waves. We further compare the TanDEM-X scene on

20   Nov. 21 with backscatter derived from a ground-based radar system in Utqiaġvik (Figure 3a and b). Due to the high incidence angle of the ground-based radar, the backscatter contrast between the ice floes and the surrounding young ice and open water is significantly greater than in the SAR imagery (see circled areas in Figure 3b).

We spatially compared the phase-derived drift speed, v_ϕ (figure 3c), with the drift speed derived from the ground-based radar, v_{gr} (arrows in Figure 3c). We further compared the two with v_{gr} projected into the look direction – the reference

25   frame of v_ϕ (Figure 3d). The v_{gr} confirms largely homogenous drift speed of the floes in the southwest direction corresponding to v_ϕ (Figure 3d). The general lower v_{gr} speed can be explained by the 2.5 h averaging window as v_{gr} is averaged over a time period when winds fluctuated between roughly 5.5 and 7 m s⁻¹ while v_ϕ was derived when winds were in the upper range near 6.5 m s⁻¹ recorded in Utqiaġvik. v_{gr} calculated in areas occupied by young ice is derived from the drift of floes occupying the respective pixels either before or after the SAR acquisition since young ice does not sustain a

30   constant signal necessary for the feature tracking algorithm used. Therefore, the match between the derived velocities v_ϕ and v_{gr} is poor in areas between floes (highlighted area in Figure 3d).

To rule out a height offset between the landfast ice and the drifting ice as a possible cause for a phase offset, we calculated the drift speed error (Equation 4) to be roughly 1 mm s^{-1} per cm height difference. Assuming first-year ice, a difference in freeboard between smooth sections of landfast and drifting ice greater than 5 cm is unlikely, since this would correspond to a difference in ice thickness of ~0.5 m and ice is unlikely to be thicker at this time of year. Based on local field analysis in

5   years with particularly rough landfast ice (e.g. spring 2015), large areas of rubble ice can potentially raise the mean InSAR-derived height by 20 cm (Dammann et al., 2017). A roughness-induced height offset can often be identified through non-homogenous phase values across the rough area due to the m-scale resolution of TanDEM-X. Even so, a maximum expected offset would therefore be roughly 25 cm and lead to a 2.5 cm s^{-1} height-induced bias, ruling out elevation differences as a substantial contributor to biases in the drift speed estimates.

10   **3.2 Evaluating fracture dynamics near Holm Land, Greenland**

From the previous section, it is clear that the interferometric phase can be accurately used to derive ice drift speed in look direction. However, due to the calibration offsets, the absolute speed cannot be resolved without stationary landfast ice or land in the image, which can serve as a calibration point for zero drift speed. Even so, relative speed can still be resolved and is potentially of great value. One example is to determine the rate at which a lead opens or closes, which is dependent on the

15   relative speed difference between the two sides of the lead. We applied InSAR to two acquisitions from the Fram Strait (Figure 4a) consisting of near continuous first- and multiyear (marked "A") sea ice and features a fracture running northwest towards Holm Land, Greenland. The main objective with this case study is to demonstrate the application to determine the opening/closing rates of fractures. In this case, it is possible to obtain absolute speed, since one of the images contains land, but this is not necessary as relative speed would be equally useful in determining opening/closing rates.

20   We calculated v_ϕ (Figure 4b) relative to the stationary ice closest to shore and define positive direction opposite to look direction. The strictly positive velocity indicates a SW velocity component. The higher speed upstream of the lead (to the NE) implies that the lead was closing at the time of the acquisition. The ice motion is not directly in response to the wind, which came from the SW at roughly 3 m s^{-1}, according to data from the European Center for Medium-Range Weather Forecasts' ERA5 reanalysis. To further investigate whether the fracture was in fact closing at the time of the TanDEM-X

25   acquisition, we compared the location of the fracture edges with a Sentinel-1 image acquired 32 minutes later (Figure 5a). We delineated a section of the fracture with easily detectible boundaries in both the Sentinel-1 and TanDEM-X scenes (Figure 5b and c respectively). This comparison enabled us to estimate the closing direction (solid lines in Figure 5c) and the angle, $\theta \approx 9.2°$, relative to the TanDEM-X look direction (dashed line in Figure 5c). Comparing the fracture width in three locations (three solid lines in Figure 5c) indicated that the fracture closed by roughly 200m (176-244 m) during the 32

30   minutes between acquisitions. This corresponds to a closing velocity of 10.9 ± 1.8 cm s^{-1}. From Figure 4b, the difference in v_ϕ across this lead (along the three solid lines) is approximately 10.0 ± 1.0 cm s^{-1}, which corresponds to an instantaneous speed difference of 10.1 ± 1.1 cm s^{-1} in the direction of lead closure. This is within ~10% of the closure rate estimated from the comparison of TanDEM-X and Sentinel-1 imagery and within the window of uncertainty. The difference could be due to

variation in the closure rate over time. At these closure speeds, the 1 km wide fracture would have closed completely within approximately 3 hours. A Sentinel image acquired 15 hours later (not shown) confirms that the lead closed.

3.3 Assessing drift zones in Vilkitsky Strait, Russia

We further examined an additional case study in the Vilkitsky Strait, an area with relevance in the context of maritime navigation, to demonstrate the use of InSAR in a dynamically complex scenario (not homogenous floe speeds as in previous sections). The Strait near Taimyr Peninsula features either landfast ice or temporarily stationary pack ice (as absence of landfast ice is apparent in ice charts by the Arctic and Antarctic Research Institute – www.aari.ru). Stationary pack ice is also present south of Bolshevik Island in Severnaya Zemlya visible with lower backscatter and zero ice drift in look direction in Figure 6a and b respectively (see "A" and "B" in Figure 6b). Between these areas of stationary ice are two distinct intermediate zones of ice moving at roughly 0.3 m s^{-1} ("C" and "D") bordering a channel with higher velocities ranging between roughly 0.35 and 0.45 m s^{-1} ("E-H"). The drift is approximately eastward in response to a WSW wind of roughly 6 m s^{-1} obtained from ERA5 reanalysis. The westerly wind leads to open water on the east side adjacent to the peninsula (see "I" in Figure 6a), allowing otherwise confined ice to move more freely leading to larger velocities ("E"). The central channel ("F"-"H") exhibits higher drift speed than the ice immediately to each side ("C" and "D") and variable speed in the form of a ramping speed ("F" and "G"), towards a prominent sinuous speed discontinuity extending northward from the peninsula ("H"). This discontinuity indicates convergence of roughly 10 cm s^{-1}, which is expected to lead to large-scale scale rafting and ridge building. However, there is no evidence of any ridges or ice rubble in the backscatter in Figure 6a. This suggests the event had only just commenced and / or was short-lived. The absence of any ridge features in the backscatter amplitude imagery suggests the process may be transient, impacting different sections of ice as it passes by the point of convergence.

The Vilkitsky Strait is known for the formation of ice arches in the springtime through the consolidation of ice with m-scale thickness. The scenario presented here may be the precursor to the formation of an ice arch where the drifting ice increasingly gets confined leading to temporarily stationary ice. Although, during December, the ice does not possess the thickness and strength to withstand the building pressure. The result is the buildup of stagnant ice under transient stress conditions as the pressure cyclically builds up and is released through ice failure. The general direction of the ice drift in the Vilkitsky Strait can be determined strictly based on the backscatter image (Figure 6a) by evaluating among other the lead at the southern margin of the strait ("I") and the apex of the partial ice arches, which points upstream ("J"). However, this example illustrates additional important utilities of this approach, namely not only to evaluate general drift direction and speed, but also to distinguish between very different dynamic regimes which cannot be evaluated strictly from the amplitude image. We have also demonstrated the ability to capture short-lived transient dynamics, which would otherwise be invisible if using InSAR with longer (> 1s) time lags.

4 Discussion – operational potential and limitations

We have demonstrated the potential use of InSAR for derivation of instantaneous sea ice drift. The phase-derived speed has shown to conform well with ground-radar validation dataset with high accuracy similar to prior InSAR validation over landfast ice using longer interferometric time lags on the scale of days to weeks (Dammann et al., 2018b). This validation

5   was limited to rigid ice floes as the young, fragmented ice did not result in a consistent backscatter signature that could be tracked with the ground-based radar. Also, the contributions to the Doppler velocity can be large and difficult to correct in areas of young ice where the ice motion is impacted by dm-scale waves. We argue that InSAR can potentially provide important drift information on the m-scale in support of operations in or near sea ice. We show here that InSAR is capable of determining the opening/closing rate of leads which can serve as important transportation corridors and may help forecast

10   travel conditions for ocean navigation. We also demonstrate the ability to identify detailed transient sea ice dynamic conditions related to convergence and deformation. Such information can possibly improve ice charting by helping to discriminate between landfast ice and temporally stationary pack ice. InSAR can also likely be utilized to evaluate interactions between sea ice and structures by quantifying strain and associated stress in a similar approach to Dammann et al. (2018b). The InSAR processing steps are well documented and can potentially be incorporated into operational analysis

15   frameworks and workflows with standard processing tools (Dammann et al., In review) such as ESA's SNAP software. Even so, important limitations exist related to the use of InSAR to detect sea ice drift.

The interferometric product only resolves one dimension (look direction) of the 2-dimensional drift; hence the actual drift speed cannot be resolved directly from the interferogram without additional interpretation steps. For surfaces experiencing consistent displacement over time periods of several hours, (e.g. glaciers) 2-D motion vectors can be estimated by data from

20   both ascending and descending passes (Lang, 2003). This is generally not the case for sea ice, but Dammann et al. (2016) demonstrated that by evaluating the coastline, persistent drift patterns, and additional coarser resolution datasets, it is possible to narrow down likely directions of ice motion. In the case of fixed installations near the coast, information related to the general drift pattern may be sufficient to determine the true velocity field. An example is Utqiaġvik, where the near-coastal sea ice predominately drifts in the orientation of the coastline. This leaves two possible directions of motion,

25   northeast and southwest, which can be discriminated from the sign of the phase values.

For operations far from shore (e.g. shipping), drift directions can be estimated based on large-scale wind data resulting in a window of possible drift directions. However, in a dense pack, ice forcing may play a larger role impacting drift direction. Here, large-scale sea ice drift products from SAR or SSM/I may be used to determine the general direction of drift. In the absence of land or fixed structures in the scene, only relative speed can be obtained since the exact speed cannot be

30   calibrated in relation to land. Even so, relative speeds are of relevance in the context of evaluating floe interaction and the opening of leads. In the case of the Fram Strait, we extracted the closing direction by comparing with Sentinel-1 imagery (Figure 5). However, even in the absence of other data, a range of likely directions can be estimated based on edge morphology. For instance, shear motion is unlikely along non-linear lead systems.

In the case of ice management (i.e. the protection of installations and drilling rigs from moving ice), the relative drift speed between a vessel and sea ice is of most relevance and can be calculated. However, this is only the case if speed of ambiguity is on the order of meters ruling out the possibility of phase ambiguities. A known vessel speed at the time of acquisition can also potentially be used to derive absolute sea ice drift speed. For the example of a closing lead in the Fram Strait, the

5 interferometric phase could be tracked continuously near the southeastern part of the image. However, in a case where a fracture caused a phase discontinuity extending all the way through the image, Δv_ϕ could theoretically not be determined since multiples of 2π could not have been discriminated. Even so, considering v_a-values reaching upwards of 1 m, would result in implausible Δv_s-values if the phase discontinuity represented a phase change of more than 2π.

The large effective baseline and h_a = 65 m results only in a minor phase change from elevation. For instance, if the ice on

10 each side of the fracture would feature a 1 cm freeboard difference, it would only result in a 0.5 mm s^{-1} drift speed error, v_e (Equation 4). However, this image features larger multiyear floes (see "A" in Figure 4a and b) causing a phase change of around 0.03 radians from surrounding ice. This implies an elevation change of roughly 30 cm and hence a difference in ice thickness of about 3 m, which is a reasonable difference between multiyear and first-year ice in this region. Ice bergs can feature even larger elevation changes than multiyear ice in which cases the sail height can end up dominating the phase

15 signal as is the case here leading to values falling outside of the color range and saturating the image (see white areas in "B" in Figure 4b). The drift speed error from multiyear ice and icebergs can thus be substantial, but such features can be easily recognized and excluded from the drift analysis.

With this work, we demonstrate that it is possible to derive instantaneous drift speed using InSAR, which can be more accurate than SAR-based approaches utilizing acquisitions separated by days, which can lead to underestimation of ice drift

20 speeds (Hutchings et al., 2011;Haller et al., 2014). However, the approach presented here merely provides a snapshot in time, hence the derived drift should be evaluated with caution and preferably used to compliment other SAR-based drift products. For instance, there may be cases where the interferograms capture ice which is being pushed in one direction creating build-up of ice forces leading to short-term rebound effects where ice motion is significantly slowed down or reversed. Although such cases will be rare, it is necessary to consider such possibilities to make sure the derived

25 instantaneous drift is representative of the general ice drift.

5 Conclusion

Sea ice is a significant component of Arctic ecosystems and its dynamic nature is of critical relevance to human near-coastal or offshore activities. Multiple techniques exist to evaluate sea ice drift across large spatial scales using remote sensing, but often with limited accuracy due to the temporal lag between satellite overpasses. We here investigate the potential of single-

30 pass TanDEM-X interferometry for deriving more accurate instantaneous drift speeds with a m-scale resolution capable of supporting stakeholders. The approach resulted in values roughly within 10 % of validation data in the form of 2.5 h drift

speed averages derived from a ground-based radar system in Utqiaġvik, Alaska. The approach was further used to determine the closing speed of a fracture in the Fram Strait. The ability of estimating the separation/closing rate of leads is an application with relevance for transportation since opening of fractures limits over-ice travel, but serves as pathways for ocean navigation.

5   Lastly, the approach was demonstrated in the Vilkitsky Strait, an important strategic location for trans-Arctic shipping as part of the northern sea route. Here, InSAR showed capable of discriminating different dynamic regimes and identify zones of shear and convergence not easily identified in the amplitude image. The case study in the Vilkitsky Strait not only demonstrates the application for InSAR-derived drift speeds, but also the ability to resolve important sea ice processes at a scale and accuracy which have been difficult to assess in the past. As an example, we were able to resolve short-lived

10   transient convergence processes otherwise invisible to SAR approaches. Such detailed information pertaining to drift speed could potentially be used to accurately determine convergence and divergence in a similar approach as applied to landfast ice. With the m-scale resolution of stripmap X-band SAR, this approach would likely be able to provide estimates of ice forcing and drift around structures relevant for engineering.

TanDEM-X is presently the only system that can produce consecutive SAR images with ms-scale temporal lag necessary to

15   derive interferometric estimates of instantaneous sea ice drift speed. The limited data availability somewhat reduces the potential for this technique in monitoring and strategic decision making, but we argue it can still be valuable in supplementing coarser-resolution datasets with higher temporal sampling where data are available. Also, with potential newer systems such as the proposed TanDEM-L mission, higher temporal resolution of drift estimates may be obtained by utilizing interferograms from multiple sensors. It is clear that single-pass InSAR is not only relevant as a tactical support tool

20   for Arctic stakeholders, but provides an important tool to assess short-term km-scale sea ice processes. Such information can help make strategic decisions by evaluating seasonal dynamics of different ice regimes as well as aid in the development and improvement of sea ice models and predictions.

Acknowledgements

This work was supported by the Swedish National Space Agency (Dnr 192/15). TanDEM-X data were provided free of

25   charge by the German Aerospace Center (DLR) through a science proposal (XTI_GLAC6921). Sentinel-1 data are provided free of charge by the European Union Copernicus program and were accessed through the Alaska Satellite Facility (ASF). The mooring observations by Utqiaġvik was supported by Arctic Research for Sustainability (ArCS) Project and Grant in Aid for Scientific Research 15H03721 from the Japanese Ministry of Education, Culture, Sports, Science, and Technology. We thank Bill Hauer at ASF, Thomas Busche at DLR, and David Duncan and Anis Elyouncha at Chalmers University of

30   Technology for valuable support and guidance.

Competing interests

The authors declare that they have no conflict of interest.

References

Ahlnäs, K., and Garrison, G.: Satellite and oceanographic observations of the warm coastal current in the Chukchi Sea, Arctic, 244-254, 1984.

Bamler, R., and Hartl, P.: Synthetic aperture radar interferometry, Inverse problems, 14, R1, 1998.

Berg, A., and Eriksson, L. E. B.: Investigation of a hybrid algorithm for sea ice drift measurements using synthetic aperture radar images, IEEE Transactions on Geoscience and Remote Sensing, 52, 5023-5033, 2014.

Berg, A., Dammert, P., and Eriksson, L. E. B.: X-Band Interferometric SAR Observations of Baltic Fast Ice, IEEE Transactions on Geoscience and Remote Sensing, 53, 1248-1256, 10.1109/TGRS.2014.2336752, 2015.

Comiso, J. C., and Hall, D. K.: Climate trends in the Arctic as observed from space, Wiley Interdisciplinary Reviews: Climate Change, 5, 389-409, 10.1002/wcc.277, 2014.

Arctic Council: Arctic marine shipping assessment, Protection of the Arctic Marine Environment Working Group (PAME), Akureyri, Island, 190, 2009.

Dammann, D. O., Eicken, H., Meyer, F., and Mahoney, A.: Assessing small-scale deformation and stability of landfast sea ice on seasonal timescales through L-band SAR interferometry and inverse modeling, Remote Sens Environ, 187, 492-504, 10.1016/j.rse.2016.10.032, 2016.

Dammann, D. O., Eicken, H., Saiet, E., Mahoney, A., Meyer, F., and George, J. C.: Traversing sea ice - linking surface roughness and ice trafficability through SAR polarimetry and interferometry IEEE Journal of Selected Topics in Applied Earth Observations and Remote Sensing, 11, 416-433, 10.1109/JSTARS.2017.2764961, 2017.

Dammann, D. O., Eicken, H., Mahoney, A., Meyer, F., and Betcher, S.: Assessing sea ice trafficability in a changing Arctic, Arctic, 71, 59-75, 10.14430/arctic4701, 2018a.

Dammann, D. O., Eicken, H., Mahoney, A., Meyer, F., Freymueller, J., and Kaufman, A. M.: Evaluating landfast sea ice stress and fracture in support of operations on sea ice using SAR interferometry, Cold Reg Sci Technol, 10.1016/j.coldregions.2018.02.001, 2018b.

Dammann, D. O., Eicken, H., Mahoney, A., Meyer, F. J., Eriksson, L. E. B., Saiet, E., Freymueller, J., and Jones, J.: New Possibilities Using TS-X and TD-X in Support of Sea Ice Use, EUSAR 2018; 12th European Conference on Synthetic Aperture Radar, 2018c, 1-6

Dammann, D. O., Eriksson, L. E. B., Mahoney, A., Stevens, C. W., Van der Sanden, J., Eicken, H., Meyer, F., and Tweedie, C.: Mapping Arctic bottomfast sea ice using SAR interferometry, Remote Sensing, 10(5), 720, 10.3390/rs10050720, 2018d.

Dammann, D. O., Eriksson, L. E. B., Mahoney, A. R., and Eicken, H.: Landfast sea ice stability – mapping pan-Arctic ice regimes with implications for ice use, subsea permafrost and marine habitats, The Cryosphere, 10.5194/tc-2018-129, In review.

Dammert, P. B. G., Lepparanta, M., and Askne, J.: SAR interferometry over Baltic Sea ice, Int J Remote Sens, 19, 3019-3037, 10.1080/014311698214163, 1998.

Dierking, W., Lang, O., and Busche, T.: Sea ice local surface topography from single-pass satellite InSAR measurements: a feasibility study, The Cryosphere, 11, 1967, 10.5194/tc-11-1967-2017, 2017.

Druckenmiller, M. L., Eicken, H., Johnson, M. A., Pringle, D. J., and Williams, C. C.: Toward an integrated coastal sea-ice observatory: System components and a case study at Barrow, Alaska, Cold Reg Sci Technol, 56, 61-72, 10.1016/J.Coldregions.2008.12.003, 2009.

Eicken, H., Lovecraft, A. L., and Druckenmiller, M. L.: Sea-Ice System Services: A Framework to Help Identify and Meet Information Needs Relevant for Arctic Observing Networks, Arctic, 62, 119-136, 10.14430/arctic126, 2009.

Eicken, H., Jones, J., Meyer, F., Mahoney, A., Druckenmiller, M. L., Rohith, M., and Kambhamettu, C.: Environmental security in Arctic ice-covered seas: from strategy to tactics of hazard identification and emergency response, Mar Technol Soc J, 45, 37-48, doi.org/10.4031/MTSJ.45.3.1, 2011.

Eicken, H., and Mahoney, A. R.: Sea Ice: Hazards, Risks, and Implications for Disasters, in: Coastal and Marine Hazards, Risks, and Disasters, edited by: Ellis, J. T., Sherman, D. J., and Shroder, J. F., Elsevier Inc., Amsterdam, Netherlands, 381-399, 2015.

Ferretti, A., Monti-Guarnieri, A., Prati, C., Rocca, F., and Massonet, D.: InSAR Principles-Guidelines for SAR Interferometry Processing and Interpretation, ESA Publications, TM-19, 2007.

Goldstein, R. M., and Werner, C. L.: Radar interferogram filtering for geophysical applications, Geophys Res Lett, 25, 4035-4038, 1998.

Haller, M., Brümmer, B., and Müller, G.: Atmosphere-ice forcing in the transpolar drift stream: results from the DAMOCLES ice-buoy campaigns 2007-2009, The Cryosphere, 8, 275, 2014.

Hutchings, J. K., Roberts, A., Geiger, C. A., and Richter-Menge, J.: Spatial and temporal characterization of sea-ice deformation, Annals of Glaciology, 52, 360-368, 2011.

Jones, J. M., Eicken, H., Mahoney, A. R., Rohith, M. V., C., K., Y., F., I., O. K., and George, J. C.: Landfast sea ice breakouts: Stabilizing ice features, oceanic and atmospheric forcing at Barrow, Alaska, Continental Shelf Research, 126, 10.1016/j.csr.2016.07.015, 2016.

Karvonen, J.: Virtual radar ice buoys–a method for measuring fine-scale sea ice drift, The Cryosphere, 10, 29-42, 2016.

Kræmer, T., Johnsen, H., and Brekke, C.: Emulating Sentinel-1 Doppler radial ice drift measurements using Envisat ASAR data, IEEE Transactions on Geoscience and Remote Sensing, 53, 6407-6418, 2015.

5 Krupnik, I., Aporta, C., Gearheard, S., Laidler, G. J., and Holm, L. K.: SIKU: knowing our ice, Springer, New York, 2010.

Kwok, R., Schweiger, A., Rothrock, D., Pang, S., and Kottmeier, C.: Sea ice motion from satellite passive microwave imagery assessed with ERS SAR and buoy motions, Journal of Geophysical Research: Oceans, 103, 8191-8214, 1998.

Kwok, R., Spreen, G., and Pang, S.: Arctic sea ice circulation and drift speed: Decadal trends and ocean currents, Journal of Geophysical

10 Research: Oceans, 118, 2408-2425, 2013.

Lang, O.: Radar Remote Sensing in Western Antarctica with Special Emphasis on Differential Interferometry, Deutsches Zentrum für Luft-und Raumfahrt, 2003.

Li, S., Shapiro, L., McNutt, L., and Feffers, A.: Application of Satellite Radar Interferometry to the Detection of Sea Ice Deformation, Journal of the Remote Sensing Society of Japan, 16, 67-77, 1996.

15 Mahoney, A., Eicken, H., Gaylord, A. G., and Gens, R.: Landfast sea ice extent in the Chukchi and Beaufort Seas: The annual cycle and decadal variability, Cold Reg Sci Technol, 103, 41-56, 10.1016/J.Coldregions.2014.03.003, 2014.

Mahoney, A., Eicken, H., Fukamachi, Y., Ohshima, K. I., Simizu, D., Kambhamettu, C., Rohith, M., Hendricks, S., and Jones, J.: Taking a look at both sides of the ice: comparison of ice thickness and drift speed as observed from moored, airborne and shore-based instruments near Barrow, Alaska, Annals of Glaciology, 56, 363-372, 2015.

20 Mahoney, A., Dammann, D. O., Johnson, M. A., Eicken, H., and Meyer, F. J.: Measurement and imaging of infragravity waves in sea ice using InSAR, Geophys Res Lett, 43, 6383–6392, 10.1002/2016GL069583 2016.

Marbouti, M., Praks, J., Antropov, O., Rinne, E., and Leppäranta, M.: A Study of Landfast Ice with Sentinel-1 Repeat-Pass Interferometry over the Baltic Sea, Remote Sensing, 9, 833, 10.3390/rs9080833, 2017.

Meier, W. N., and Maslanik, J. A.: Effect of environmental conditions on observed, modeled, and assimilated sea ice motion errors,

25 Journal of Geophysical Research: Oceans, 108, 2003.

Meier, W. N., Hovelsrud, G. K., Oort, B. E., Key, J. R., Kovacs, K. M., Michel, C., Haas, C., Granskog, M. A., Gerland, S., and Perovich, D. K.: Arctic sea ice in transformation: A review of recent observed changes and impacts on biology and human activity, Reviews of Geophysics, 52, 185-217, 2014.

Meyer, F. J., Mahoney, A. R., Eicken, H., Denny, C. L., Druckenmiller, H. C., and Hendricks, S.: Mapping arctic landfast ice extent using

30 L-band synthetic aperture radar interferometry, Remote Sens Environ, 115, 3029-3043, 10.1016/J.Rse.2011.06.006, 2011.

Morris, K., Li, S., and Jeffries, M.: Meso-and microscale sea-ice motion in the East Siberian Sea as determined from ERS-I SAR data, Journal of Glaciology, 45, 370-383, 1999.

Muckenhuber, S., and Sandven, S.: Open-source sea ice drift algorithm for Sentinel-1 SAR imagery using a combination of feature tracking and pattern matching, The Cryosphere, 11, 1835, 2017.

35 Norton, D. W., and Gaylord, A. G.: Drift velocities of ice floes in Alaska's northern Chukchi Sea flaw zone: Determinants of success by spring subsistence whalers in 2000 and 2001, Arctic, 347-362, 2004.

Oikkonen, A., Haapala, J., Lensu, M., and Karvonen, J.: Sea ice drift and deformation in the coastal boundary zone, Geophys Res Lett, 43, 2016.

Rampal, P., Weiss, J., and Marsan, D.: Positive trend in the mean speed and deformation rate of Arctic sea ice, 1979–2007, Journal of

40 Geophysical Research: Oceans, 114, 10.1029/2008JC005066, 2009a.

Rampal, P., Weiss, J., Marsan, D., and Bourgoin, M.: Arctic sea ice velocity field: General circulation and turbulent-like fluctuations, Journal of Geophysical Research: Oceans, 114, 2009b.

Rohith, M., Jones, J., Eicken, H., and Kambhamettu, C.: Extracting quantitative information on coastal ice dynamics and ice hazard events from marine radar digital imagery, IEEE Transactions on Geoscience and Remote Sensing, 51, 2556-2570, 2013.

45 Romeiser, R., and Thompson, D. R.: Numerical study on the along-track interferometric radar imaging mechanism of oceanic surface currents, IEEE transactions on geoscience and remote sensing, 38, 446-458, 2000.

Romeiser, R., and Runge, H.: Theoretical evaluation of several possible along-track InSAR modes of TerraSAR-X for ocean current measurements, IEEE Transactions on Geoscience and Remote Sensing, 45, 21-35, 2007.

Romeiser, R., Suchandt, S., Runge, H., Steinbrecher, U., and Grunler, S.: First analysis of TerraSAR-X along-track InSAR-derived current

50 fields, IEEE Transactions on Geoscience and Remote Sensing, 48, 820-829, 2010.

Scheiber, R., De Zan, F., Prats, P., Araújo, L. S. A., Künemund, M., and Marotti, L.: Interferometric sea ice mapping with TanDEM-X: First experiments, Geoscience and Remote Sensing Symposium (IGARSS), 2011 IEEE International, 2011, 3594-3597

Shirasawa, K., Ebuchi, N., Leppäranta, M., and Takatsuka, T.: Ice-edge detection from Japanese C-band radar and high-frequency radar coastal stations, Annals of Glaciology, 54, 59-64, 10.3189/2013AoG62A007, 2013.

55 Spreen, G., Kwok, R., and Menemenlis, D.: Trends in Arctic sea ice drift and role of wind forcing: 1992–2009, Geophys Res Lett, 38, 2011.

Stroeve, J. C., Serreze, M. C., Holland, M. M., Kay, J. E., Malanik, J., and Barrett, A. P.: The Arctic's rapidly shrinking sea ice cover: a research synthesis, Climatic Change, 110, 1005-1027, 10.1007/S10584-011-0101-1, 2012.

Thomas, D. N.: Sea ice, John Wiley & Sons, Chichester, United Kingdom, 2017.

Thompson, D. R., and Jensen, J.: Synthetic aperture radar interferometry applied to ship-generated internal waves in the 1989 Loch Linnhe experiment, Journal of Geophysical Research: Oceans, 98, 10259-10269, 1993.

Valenzuela, G. R.: Theories for the interaction of electromagnetic and oceanic waves—A review, Boundary-Layer Meteorology, 13, 61-85, 1978.

Vincent, F., Raucoules, D., Degroeve, T., Edwards, G., and Abolfazl Mostafavi, M.: Detection of river/sea ice deformation using satellite interferometry: limits and potential, Int J Remote Sens, 25, 3555-3571, 2004.

Werner, C., Wegmüller, U., Strozzi, T., and Wiesmann, A.: Gamma SAR and interferometric processing software, Proceedings of the ERS-ENVISAT symposium, Gothenburg, Sweden, 2000, 1620

Winsor, P., and Chapman, D. C.: Pathways of Pacific water across the Chukchi Sea: A numerical model study, Journal of Geophysical Research: Oceans, 109, 2004.

Zhang, J., Thomas, D., Rothrock, D., Lindsay, R., Yu, Y., and Kwok, R.: Assimilation of ice motion observations and comparisons with submarine ice thickness data, Journal of Geophysical Research: Oceans, 108, 2003.

Zhang, J., Lindsay, R., Schweiger, A., and Rigor, I.: Recent changes in the dynamic properties of declining Arctic sea ice: A model study, Geophys Res Lett, 39, 10.1029/2012GL053545, 2012.
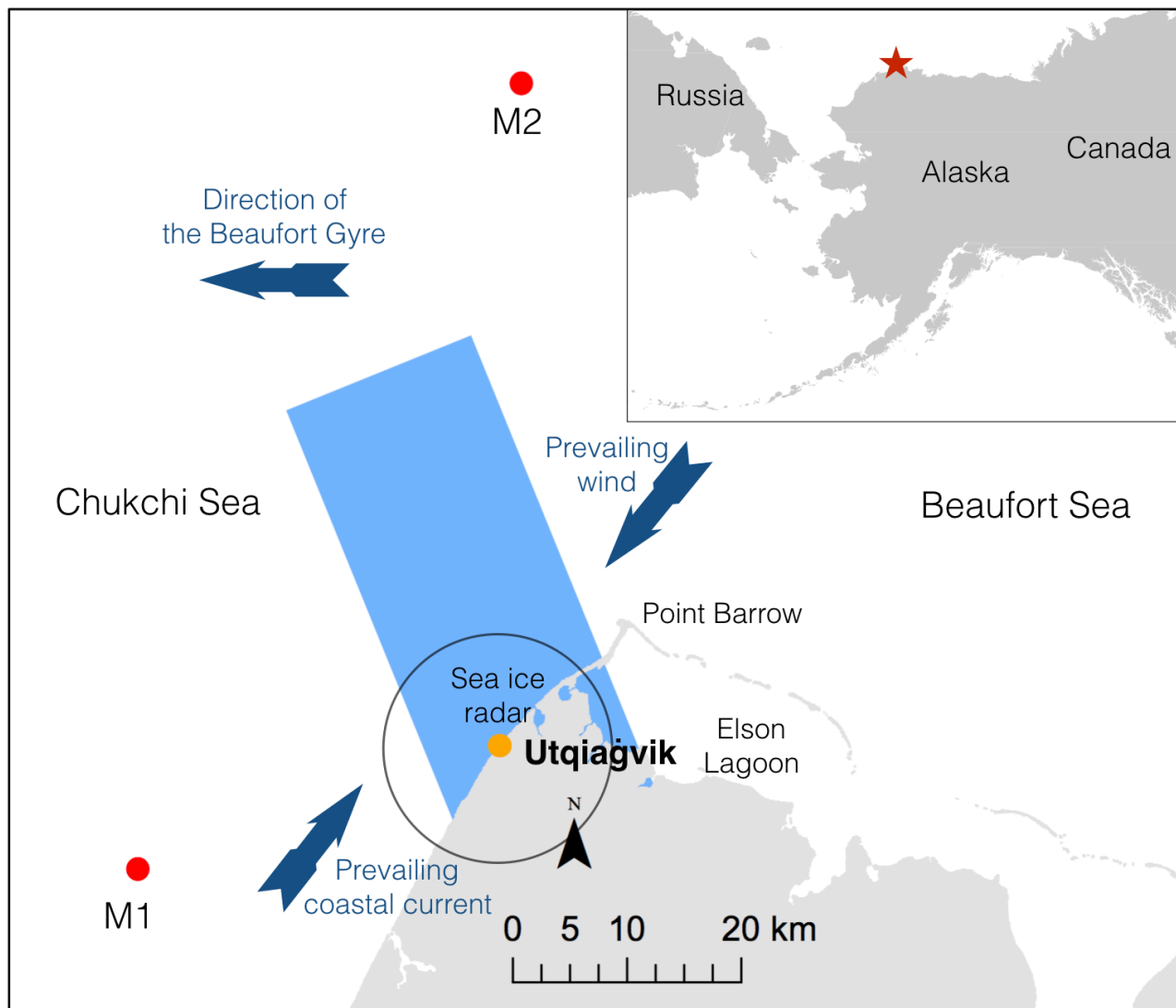
Figure 1: Overview of study region near Utqiaġvik, Alaska. The blue rectangle signifies the footprint of the SAR acquisitions and the circle marks the range of the ground-based radar (yellow dot). Red dots signify location of deployed moorings for assessing ocean surface current.
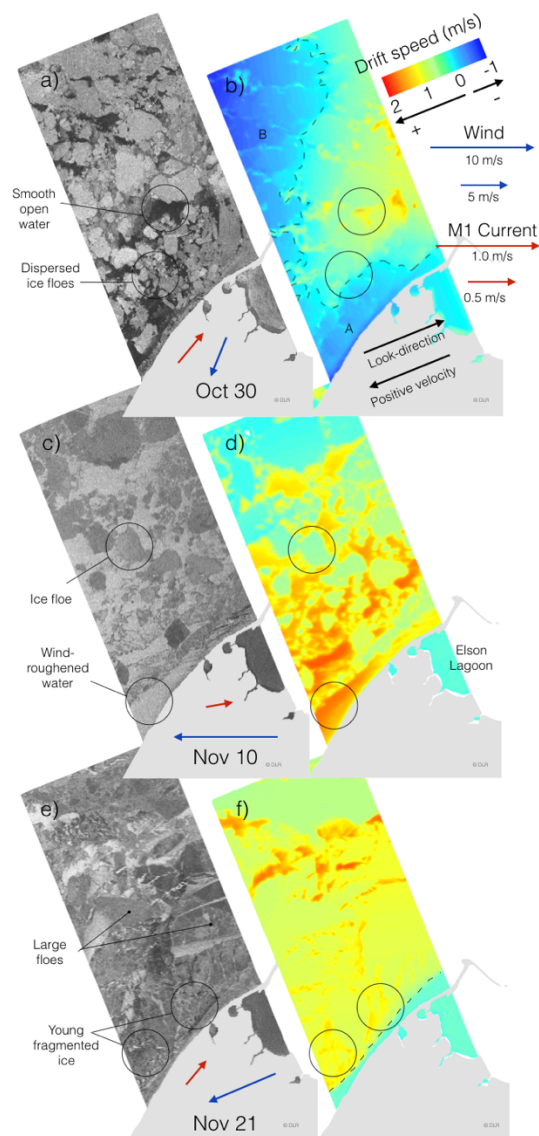
5   **Figure 2: Three TanDEM-X backscatter images individually stretched to emphasize different ice types and features (left column) and phase-derived speed in look direction (right column) by Utqiaġvik during fall 2015 at 03:19 UTC. Positive velocity is defined opposite of look direction. Line of zero velocity is marked with a dashed line. Velocity of wind (recorded in Utqiaġvik) and currents (at M1) at the time of acquisition are indicated with blue and red arrows respectively. Land is masked out in light gray. A and B indicate areas of negative velocity in (a) further discussed in the text.**
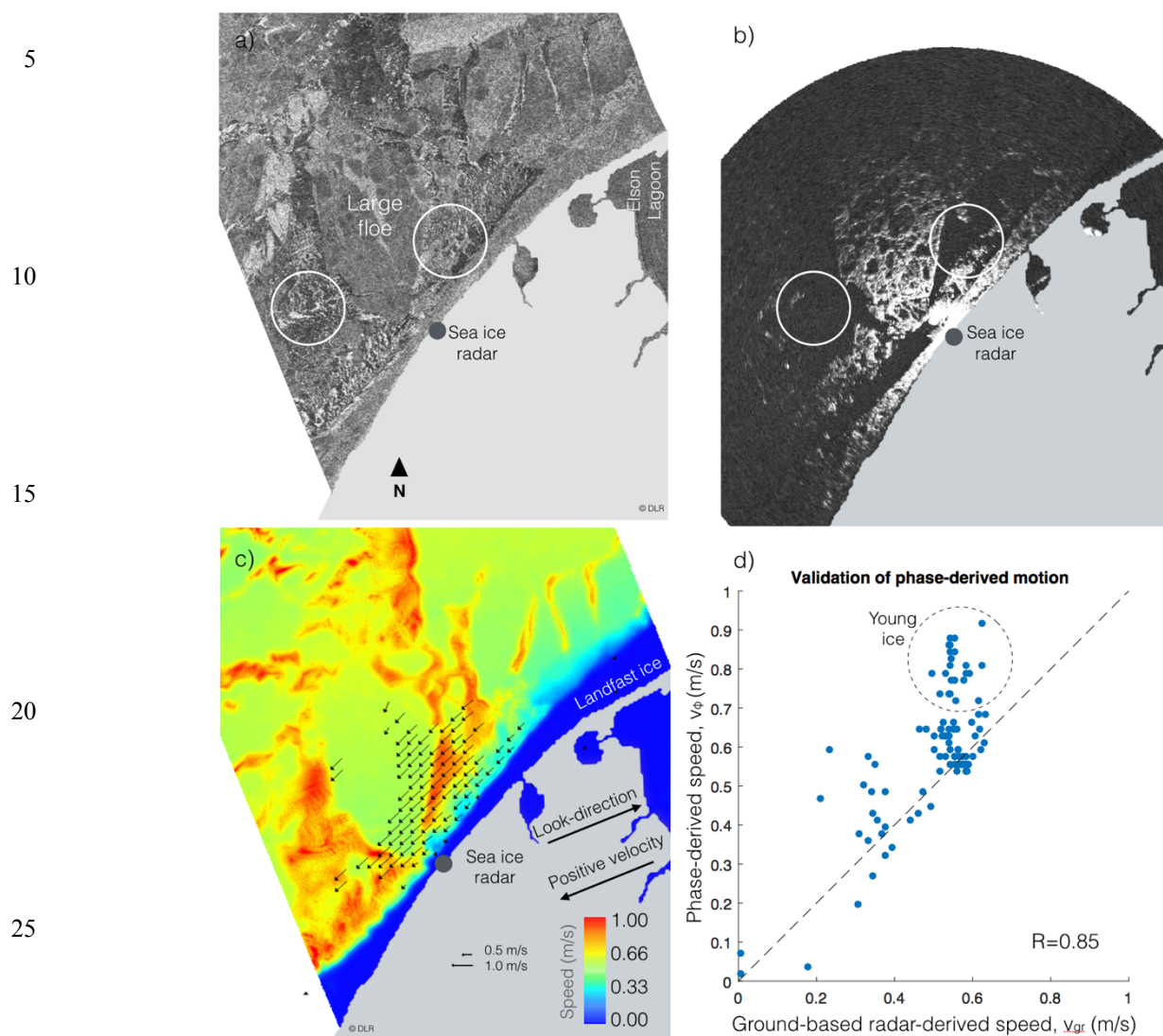
Figure 3: (a) TanDEM-X backscatter scene over Utqiaġvik, Alaska on 21 Nov 2015 3:19 UTC. **(b)** ground-based radar backscatter scene 21 Nov 2015 3:18 UTC. Circles indicate areas of young ice hence reduced backscatter in (b). **(c)** interferometric phase-derived look-directional speed at 3:19 UTC. Arrows represent speed derived from ground-based radar data averaged between 1:52 – 4:28 UTC. Land is masked out in light gray. **(d)** Comparison between look-directional speed as evaluated using InSAR- and ground-based radar-derived speed. Circle in (d) indicates poor match between motion products in areas with young sea ice and reduced backscatter from the ground-based radar predominately within the right circled area in (a) and (b).
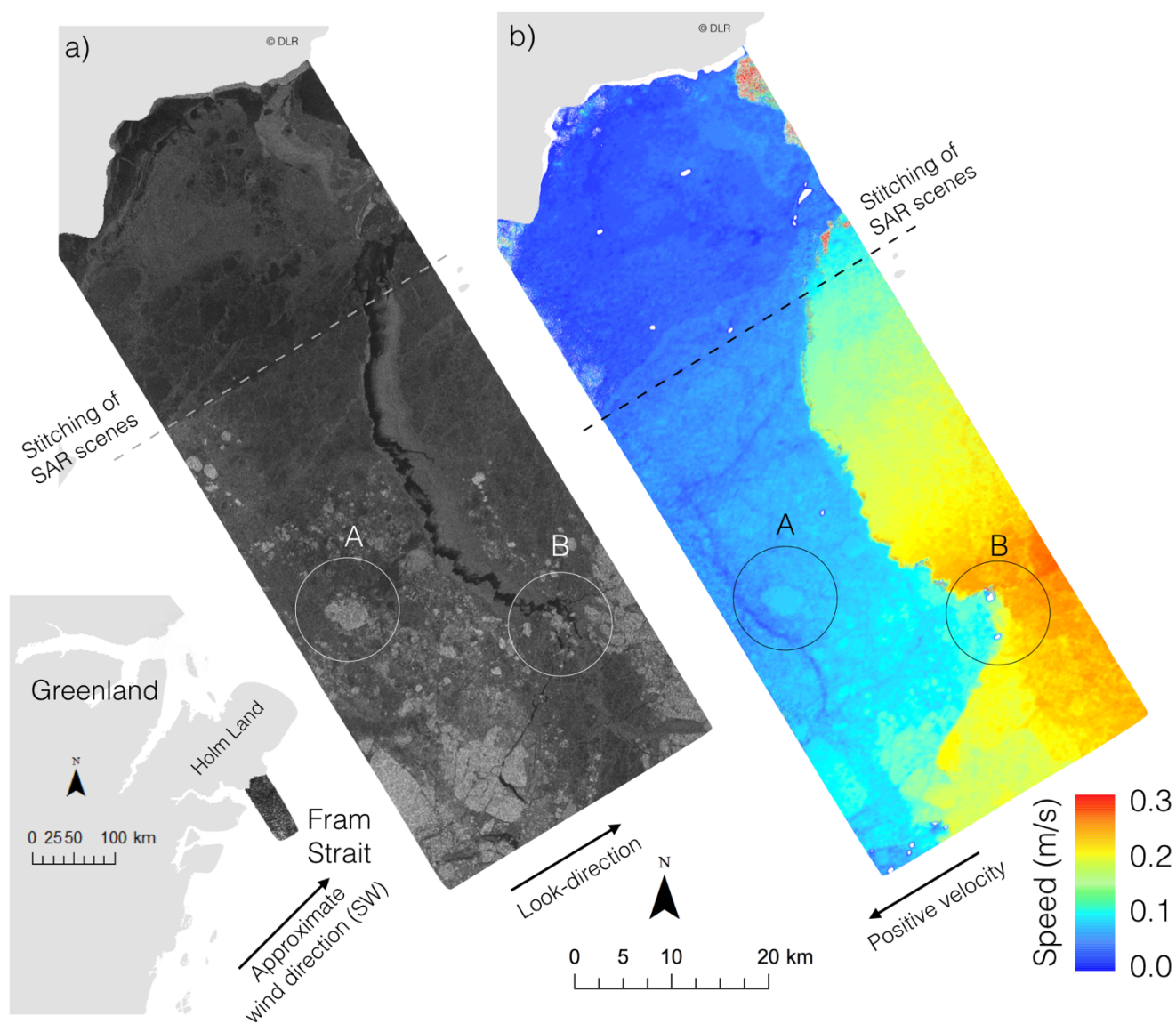
Figure 4: (a) TanDEM-X backscatter scene over Fram Strait 23 Nov 2015 at 17:00 UTC. **(b)** Look-directional component of InSAR-derived speed. Letters signify multiyear ice "A" and area of ice bergs "B". Land is masked out in light gray. Wind at the time of the acquisition was roughly southwesterly at 3 m/s.
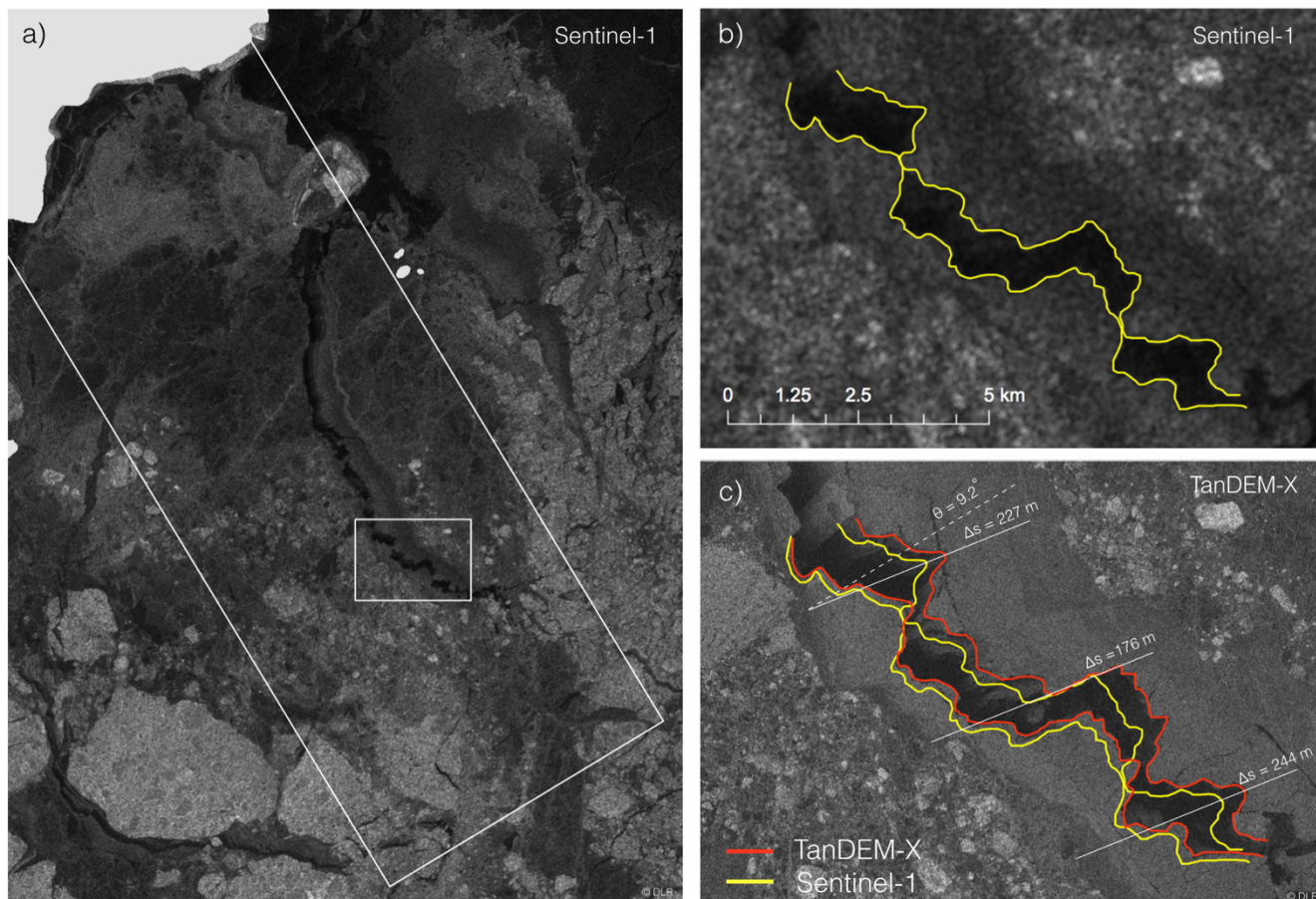
Figure 5: (a) Sentinel-1 backscatter image acquired 23 Nov 2015 at 17:32 UTC. The large white box represents the areal extent of the TanDEM-X image. (b) outlined part of the fracture (yellow line) as observed with Sentinel-1 within the small rectangle in (a). (c) outlined part of the fracture (red line) as observed with TanDEM-X. Width of the fracture (Δs) is compared along the solid lines and θ represents angle between opening direction (solid lines) and the TanDEM-X look direction (dashed line). Land is masked out in light gray.
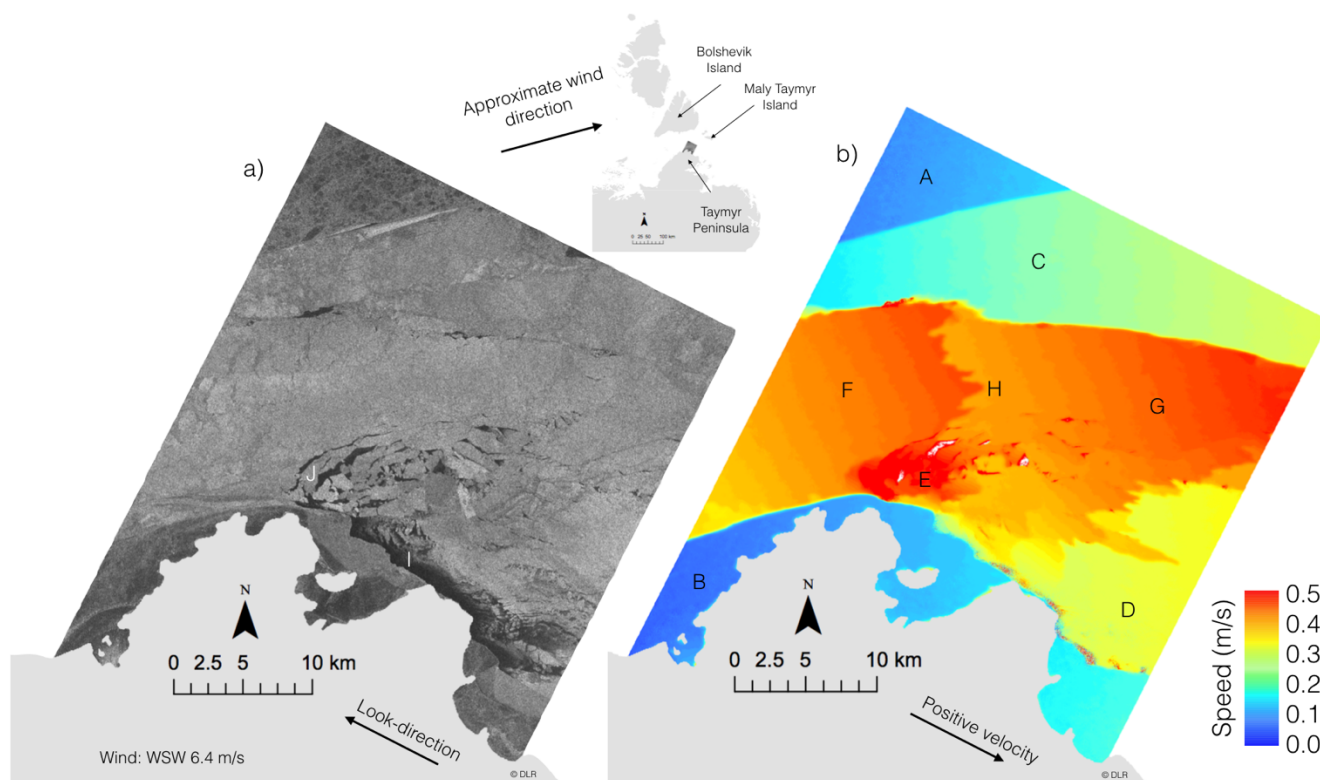
Figure 6: (a) TanDEM-X backscatter scene over Vilkitsky Strait 17 Dec 2013. (b) Look-directional component of InSAR-derived speed. Land is masked out in light gray. Wind at the time of the acquisition was roughly WSW at 6 m/s. Letters signify different dynamic regions described in the text.

Table 1: List of TanDEM-X datasets analyzed

Region	Orbit /cycle	Date	Dir.	$B_\parallel$ (m)	θ	v_a (m s^{-1})
Utqiaġvik	46609/ 279	30 Oct 2015	A	89.2	20.9	3.70
Utqiaġvik	46776/ 280	10 Nov 2015	A	42.6	20.9	7.76
Utqiaġvik	46943 / 281	21 Nov 2015	A	73.3	20.9	4.51
Fram Str.	46982 / 281	23 Nov 2015	A	69.5	32.5	3.16
Fram Str.	46982 / 281	23 Nov 2015	A	69.5	32.5	3.16
Vilkitsky Str.	36253 / 217	17 Dec 2013	D	152.2	38.5	1.24

Dir. = **orbit direction either ascending (A) or descending (D)**, $B_\parallel$ = **along-track baseline**, θ = **incidence angle, and** v_a = **speed of**
5   **ambiguity**